Indentation in single-crystal 6H silicon carbide: Experimental investigations and finite element analysis

Ka Ho Pang[a], Emil Tymicki[b], Anish Roy[1a]

[a]Wolfson School of Mechanical, Electrical and Manufacturing Engineering, Loughborough University, LE11 3TU, The UK

[b]Institute of Electronic Materials Technology, ul. Wólczyńska 133, 01-991 Warsaw, Poland

Abstract

Silicon carbide (SiC) is a promising material ideally suited for small-scaled devices deployed in harsh environments. SiC is brittle in bulk form, however, at small component length-scales plasticity is observed. A good understanding of deformation behaviour is, therefore, crucial for reliable small-scale component design and fabrication. Here, experimental and numerical analysis of the deformation behaviour of single-crystal 6H-SiC in nanoindentation is presented. Nanoindentation studies are carried out in two orientations of the single-crystal using a Berkovich indenter. Next, a crystal-plasticity theory was implemented in finite-element (FE) modelling framework to predict the deformation of the hexagonal single-crystal. The validity of the present FE modelling methodology was corroborated through comparison between FE simulations and experimental data in terms of indent profile and load-displacement curves. Our results showed that classical crystal plasticity theory can be reliably applied in predicting plastic deformation of ceramic at small scales.

---

[1] Corresponding author,
E-mail address: A.Roy3@lboro.ac.uk

1 Introduction

Silicon carbide (SiC) is an excellent structural material for microelectromechanical systems (MEMS) applications due to its outstanding mechanical, chemical, and electrical properties. Such devices are ideally suited for harsh environment applications [1] which include high temperature (>600°C), high mechanical wear, high radiation, high oxidation, and corrosive environments. Although crystalline SiC is a polymorphic material that exists in well over 100 distinct polytypes [2], the hexagonal 6H-SiC polytype is technologically relevant for MEMS applications since it can be reliably produced in high-volumes with good quality [3,4]. Component manufacture requires machining of SiC, which becomes a challenge, due to the material's excellent mechanical properties. Thus, a good understanding of deformation mechanisms in micro-machining is crucial for appropriate component manufacture and assembly.

To date, extensive research has been conducted on the ductile regime micro-machining of SiC including single point diamond turning (SPDT) [5,6], grinding [7,8] and nanoscratching [9,10]. There are two reported causes for ductile regime machining in SiC: (1) due to high pressure phase transformation (HPPT), or, (2) due to dislocation-assisted plasticity. Patten and co-workers [11] proposed that the ductile material removal mechanism in SPDT process was due to HPPT according to the amorphous appearance of the chips. However, strong evidence on the existence of the amorphous phase (such as halo ring pattern under TEM diffraction) was lacking in their study. In contrast, experiment on diamond turning of reaction-bonded silicon carbide reveal no phase transformation of 6H-SiC grains [12], which indicate dislocation-assisted plasticity is the major deformation mechanisms for the observed ductile response. Xiao and co-workers [13] suggest that the ductile response for 6H-SiC is a combination of HPPT and dislocation slip with the former contributing less to the overall effect. Their studies indicate that evolution of Frank partial dislocations and basal

plane edge dislocations are the primary cause for the ductile deformations. Nanoindentation on 6H-SiC (0001) with a Vickers indenter show plastic deformation without cracks up to 400mN [8]. TEM studies on the imprint of single-crystal 6H-SiC induced by a sharp Berkovich indenter show basal plane dislocation activity with possible cross slip near the indented area [14]. Page and co-workers [15,16] also perform TEM experiment on the imprints of the nanoindentation with Berkovich indenter at loads ranging from 1.5 mN to 100 mN and suggested that the increased in dislocation density is solely due to the dislocation slip. Datye and co-workers [17] have studied the effective modulus and hardness at four different crystallographic orientations by combining experiment and crystal plasticity modelling. Their study suggest that basal slip dominates plastic deformation with its corresponding critical resolved shear stress (CRSS) being ~4.8 GPa. It is acknowledged that indentation studies indicate 6H-SiC possess weak anisotropy primarily due to the lack of slip activity on multiple slip systems. However, it is understood that non-basal slip system do contribute to overall deformations. A thorough understanding of the plastic deformation mechanisms especially the slip activation sequence in single-crystal SiC is lacking, which we intend to study here.

Specifically, we carry out an experimental and numerical study of nanoindentation in single-crystal 6H-SiC. The paper is organised as follows: experimental studies including sample preparation is described in Section 2. Description of the theoretical framework of the crystal plasticity theory is in Section 3, followed by details of the numerical modelling procedure used to simulate the indentation process in section 4. Detailed analysis and discussion elucidating the deformation mechanisms in 6H-SiC is in section 5. We conclude with some remarks in Section 6.

2 Experimental analysis

2.1 Sample preparation

Single-crystal 6H-SiC specimens manufactured by Institute of Electronic Materials Technology, Poland were used in this study. The 6H-SiC single-crystal was grown by seeded physical vapour transport method (PVT) with open back side seed method[18]. The crystallization processes ran in furnace equipped with a single-section resistance graphite heater. The crystal grows on 2'' Si-faced 6H-SiC seed wafer with an orientation of (0001). The growth chamber was placed in axially symmetrical temperature field. The temperature during the processes was measured by two pyrometers: one directed at the bottom of heater (pointing about 2250 °C) and another directed at the top of the crystal holder closing the crucible (pointing about 2170 °C). The distance between seed and source material in the very first stage of growth was 50 mm which decreased to 40 mm during the crystallization process. The growth atmosphere was a mixture of nitrogen and argon in the proportion of 3:100. The pressure of the growth atmosphere was decreased in two-steps. In the first step, the pressure is reduced from 600 mbar to 300 mbar for 6 hours. Followed by, a decrease in pressure to 40 mbar in 10 hours.

Two single-crystal samples at different orientations were prepared for this study. The first specimen with dimension 5mm × 5mm × 0.7mm was oriented such that indentation could be performed on the basal plane (0001) (Fig. 1(a)). We refer to this orientation as 'orientation 1'. The second sample, with dimension of 2mm × 5mm × 2mm, was prepared such that the indentation axis was oriented at 45 ° to the basal plane, henceforth, referred to as 'orientation 2' (Fig. 1(b)). For orientation 2, the crystal was mounted on a special turntable, which allow for a tilt of 45˚. After cutting, all samples were checked by goniometer using x-ray diffraction. All samples were polished by diamond slurry with decreasing grain size from 16 μm, 9 μm, 6 μm to 1 μm for 30 minutes at each stages to achieve an epi-ready

surface quality. The surface roughness (R_a) of the samples after polishing is less than 2 nm. The initial dislocation density was assessed after etching the sample surface in KOH at 450⁰C for 20 minutes. Figure 2 shows the various dislocation and defect features in the sample. A software was used to evaluate the density based from this picture. The dislocation density in the samples is assessed to be $5 \times 10^4 \mathrm{cm}^{-2}$.

The lattice constants of a unit cell of single-crystal 6H-SiC were measured using single-crystal X-ray diffractometer (Bruker APEX II). The lattice parameters *a* and *c* were measured to be 3.08 Å and 15.22 Å, respectively.
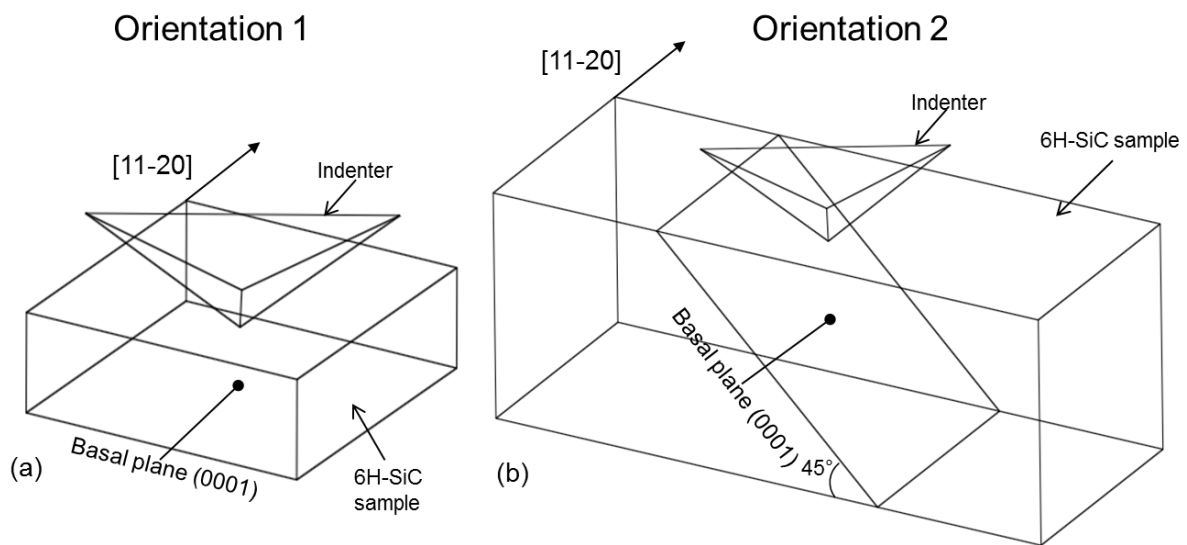

Fig 1. Schematic of indentation directions with respect to crystal orientations (a) Orientation 1: on the (0001); and (b) Orientation 2: 45° to (0001)
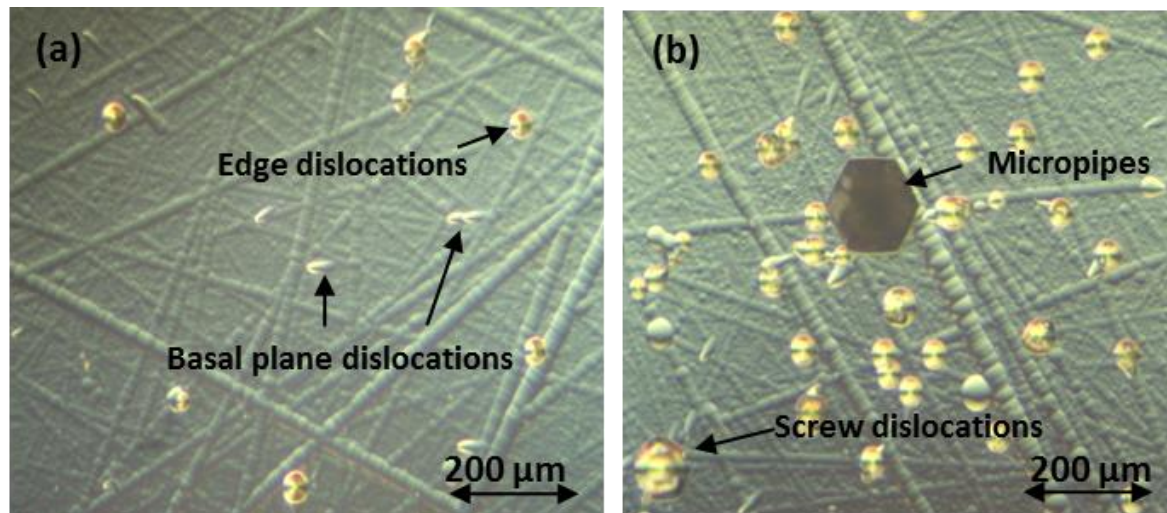
Fig 2. Light microscopy showing features in the sample after etching: (a) Edge and Basal plane dislocations and (b) Micropipes and Screw dislocations.

2.2 Experimental procedure

All the nanoindentation tests in this section were conducted on a Nano Test system (Micro Materials Ltd.) equipped with a diamond Berkovich indenter with centreline-to-face angle of 65.27° and the tip radius measured to be 400 nm. A fixed time-maximum load controlled experimental procedure was employed for all quasi-static nanoindentation studies. All the experiments were conducted under a constant maximum load at 30 mN with loading time, dwell time and unloading time equal to 100 s, 10 s and 50 s, respectively. For each test, nanoindentation was performed five times and consistent load-displacement curves were obtained each time. Here, results for a representative set of experiment are presented for each sample. After the nanoindentation experiment, the surface topography of the residual imprint was acquired with an atomic force microscope (AFM).

3 Single-crystal plasticity theory

Numerical studies based on crystal plasticity theory has been used extensively in modelling the deformation mechanisms in hexagonal closed packed (HCP) metallic material [19–21]. The technique has been used to model a host of nano-micro experimental studies

including nanoindentation [22–24]. Recent study also show that the crystal plasticity framework is applicable in modelling ceramic materials which possess HCP crystalline structures [17].

For the convenience of reader, the crystal-plasticity theory adopted in this study is described in short [25]. A deformation gradient, $\mathbf{F}$, is a composition of elastic and plastic parts:

$$\mathbf{F} = \mathbf{F_e}\mathbf{F_p}, \tag{1}$$

where the subscripts '$\mathbf{e}$' and '$\mathbf{p}$' denote the elastic and plastic part respectively. The rate of total deformation gradient, $\dot{\mathbf{F}}$, can be obtained by applying the product rule of differentiation as

$$\dot{\mathbf{F}} = \dot{\mathbf{F}}_\mathbf{e}\mathbf{F_p} + \mathbf{F_e}\dot{\mathbf{F}}_\mathbf{p}. \tag{2}$$

The velocity gradient, $\mathbf{L}$, is expressed as $\mathbf{L} = \dot{\mathbf{F}}\mathbf{F^{-1}}$, which can be further expressed as

$$\mathbf{L} = \dot{\mathbf{F}}_\mathbf{e}\mathbf{F_e^{-1}} + \mathbf{F_e}(\dot{\mathbf{F}}_\mathbf{p}\mathbf{F_p^{-1}})\mathbf{F_e^{-1}} = \mathbf{L_e} + \mathbf{L_p} . \tag{3}$$

In classical crystal plasticity theory, the plastic part of velocity gradient, $\mathbf{L_p}$, is assumed to be solely induced by shearing on each slip system in a crystal. Hence, $\mathbf{L_p}$ is related to the sum of slipping rate on all the slip systems, i.e.

$$\mathbf{L_p} = \sum_{\alpha=1}^{N}\dot{\gamma}^{(\alpha)}\mathbf{s}^{(\alpha)} \otimes \mathbf{m}^{(\alpha)}, \tag{4}$$

where N is the total number of slip systems, $\dot{\gamma}^{(\alpha)}$ is the shear slip rate on the α slip system, and $\mathbf{s}^{(\alpha)}$ and $\mathbf{m}^{(\alpha)}$ are the unit vectors of the slip direction and the normal to the slip plane in the deformed configuration respectively. The velocity gradient in the current state can be expressed as

$$\mathbf{L} = \mathbf{D} + \mathbf{W} = (\mathbf{D_e} + \mathbf{W_e}) + (\mathbf{D_p} + \mathbf{W_p}). \tag{5}$$

where, $\mathbf{D}$, is the symmetric rate of stretching and, $\mathbf{W}$, is the antisymmetric rate of spin.

From eqs.(3), (4) & (5), the following relations can be deduced

$$\mathbf{D_e} + \mathbf{W_e} = \dot{\mathbf{F}}_\mathbf{e}\mathbf{F}_\mathbf{e}^{-1};$$
$$\mathbf{D_p} + \mathbf{W_p} = \sum_{\alpha=1}^{N} \dot{\gamma}^{(\alpha)}\mathbf{s}^{(\alpha)} \otimes \mathbf{m}^{(\alpha)}.$$

(6)

The constitutive law is formulated as the relationship between the elastic part of the symmetric rate of stretching, $\mathbf{D_e}$, and the Jaumann rate of Cauchy stress, $\overset{\triangledown}{\boldsymbol{\sigma}}$, after Huang [26]

$$\overset{\triangledown}{\boldsymbol{\sigma}} + \boldsymbol{\sigma}(\mathbf{I}:\mathbf{D_e}) = \mathbf{C}:\mathbf{D_e},$$

(7)

where, $\mathbf{I}$ is the second-order identical tensor, $\mathbf{C}$ is the fourth-order elastic moduli tensor. The Jaumann stress rate is expressed as

$$\overset{\triangledown}{\boldsymbol{\sigma}} = \dot{\boldsymbol{\sigma}} - \mathbf{W_e}\boldsymbol{\sigma} + \boldsymbol{\sigma}\mathbf{W_e}.$$

(8)

The resolved shear stress, $\tau^{(\alpha)}$, on each slip system α, can be expressed according to Schmid law as,

$$\tau^{(\alpha)} = \mathbf{sym}(\mathbf{s}^{(\alpha)} \otimes \mathbf{m}^{(\alpha)}):\boldsymbol{\sigma}.$$

(9)

Following the power law proposed by Hutchinson [27], the shear rate, $\dot{\gamma}^{(\alpha)}$, is related to the resolved shear stress, $\tau^{(\alpha)}$, on the slip system α as,

$$\dot{\gamma}^{(\alpha)} = \dot{\gamma}_0 \left|\frac{\tau^{(\alpha)}}{g^{(\alpha)}}\right|^n \mathrm{sgn}(\tau^{(\alpha)}),$$

(10)

where, $\dot{\gamma}_0$ is the reference shear rate, $g^{(\alpha)}$ is the slip resistance and n is the rate-sensitivity parameter. The strain hardening is characterised by the evolution of strength, $g^{(\alpha)}$, by the relation

$$\dot{g}^{(\alpha)} = \sum_{\beta=1}^{N} h_{\alpha\beta}\left|\dot{\gamma}^{(\beta)}\right|,$$

(11)

where $h_{\alpha\beta}$ is the slip hardening modulus. Here, $h_{\alpha\alpha}$ (no sum over slip systems) and $h_{\alpha\beta}$ ($\alpha \neq \beta$) are called self and latent hardening moduli respectively. Following the work of

Peirce et al. [11] and Asaro [29,30], the self and latent moduli can be calculated in a simple form,

$$h_{\alpha\alpha} = h_0 \text{sech}^2 \left| \frac{h_0 \gamma}{\tau_S - \tau_0} \right|,$$
$$h_{\alpha\beta} = q h_{\alpha\alpha} (\alpha \neq \beta) \qquad . \tag{12}$$

where h_0 and h_s are the initial and saturated hardening moduli, q is the latent hardening ratio, τ_0 and τ_S are the shear stresses at the onset of yield and the saturation of hardening respectively. The accumulative shear strain over all slip systems, γ, can be expressed as

$$\gamma = \sum_\alpha \int_0^t \left| \dot{\gamma}^{(\alpha)} \right| dt \qquad . \tag{13}$$

4 Finite element modelling

A three-dimensional (3D) finite element (FE) model was developed to simulate the nanoindentation process. Here, we use the general purpose FE modelling software ABAQUS/Explicit v6.14 by incorporating a user subroutine VUMAT. The objective rate was based on the Green-Naghdi stress rate in ABAQUS/Explicit environment. Therefore, a conversion algorithm was required to convert the Jaumann objective rates as described in the in the constitutive law. Details of its implementation is available in [25].

The work-piece was meshed using eight-node brick elements (C3D8). In order to improve accuracy, a finer mesh was used in regions in the vicinity of the indented area (Fig. 3(a)). The total number of elements of the work piece material was around 23000. A mesh sensitivity analysis was carried out to ensure the mesh density was sufficient for the problem at hand. The modelled Berkovich indenter was identical to the one used in the experiment (see fig. 3(b)). For all practical purpose, the indenter was assumed to be rigid. To account for

the deformation in 6H-SiC, a HCP crystallographic structure was incorporated. Table 1 list a total of 30 slip systems in the five sets of slip families available in HCP crystals. Here, deformation twinning was not considered as there is no experimental evidence of deformation twining observed in indentation of single crystal 6H-SiC. Additionally, indentation studies in materials which are known to be heavily influenced by twinning such as in Mg, shown that neglecting twinning in numerical models do not affect its predictive capability for small indentation depths and imprint sizes [31], which is comparable to the indentation depths in our study. We have calibrated the model based on the experiments conducted in this study. We compare numerical results from our studies with results based on data provided in the literature [17]. In the simulation, indentions were performed by displacing the indenter in −y direction by a maximum displacement of 207 nm in 10 s. This roughly corresponds to an imposed load of 30 mN (as per the experiment). Next, the unloading step is initiated which is accomplished in 5 s. All computations were performed on a 6 core high performance computing cluster at Loughbourgh University with each computation requiring approximately 10 hours to complete.
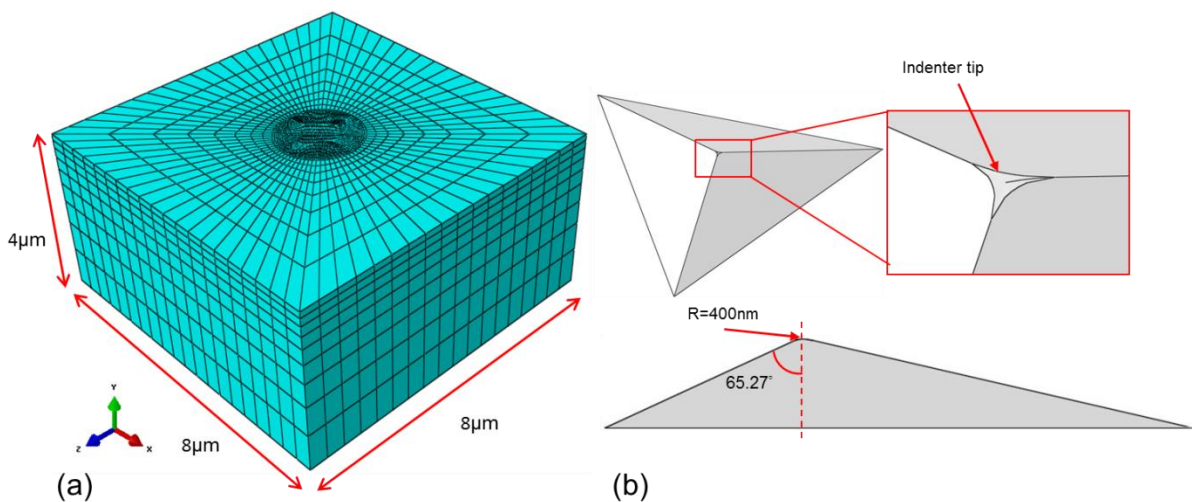

Fig. 3 (a) Finite-element model for simulation (b) geometry of the Berkovich indenter

The material properties including the CRSS of the various slip systems are listed in Table 2.

In the present study, the latent hardening parameter, q, for all the slip systems was assumed to

be 1.0 (prior studies in numerical modelling of single crystal HCP Mg show that assuming

$q = 1.0$ is acceptable [31]). Other relevant data was obtained from the literature [32] and calibration tests performed for orientation 1.

Table 1 Five sets of slip systems in HCP-like single-crystal 6H-SiC

Slip systems	#	$\mathbf{s}^{(\alpha)}$	$\mathbf{m}^{(\alpha)}$		#	$\mathbf{s}^{(\alpha)}$	$\mathbf{m}^{(\alpha)}$		#	$\mathbf{s}^{(\alpha)}$	$\mathbf{m}^{(\alpha)}$
Basal	1	$1\bar{2}10$	0001		13	$\bar{2}113$	$10\bar{1}1$		25	$\bar{2}113$	$\bar{2}112$
	2	$2\bar{1}\bar{1}0$	0001		14	$\bar{1}\bar{1}23$	$10\bar{1}1$		26	$\bar{1}2\bar{1}3$	$1\bar{2}12$
	3	$11\bar{2}0$	0001		15	$\bar{1}\bar{1}23$	$01\bar{1}1$	Pyramidal \<c+a\> 2nd order	27	$\bar{1}\bar{1}23$	$11\bar{2}2$
Prismatic	4	$1\bar{2}10$	$10\bar{1}0$		16	$1\bar{2}13$	$01\bar{1}1$		28	$\bar{2}113$	$2\bar{1}\bar{1}2$
	5	$2\bar{1}\bar{1}0$	$01\bar{1}0$		17	$1\bar{2}13$	$\bar{1}101$		29	$1\bar{2}13$	$\bar{1}2\bar{1}2$
	6	$11\bar{2}0$	$\bar{1}100$	Pyramidal \<c+a\> 1st order	18	$2\bar{1}\bar{1}3$	$\bar{1}101$		30	$11\bar{2}3$	$\bar{1}\bar{1}22$
Pyramidal \<a\>	7	$1\bar{2}10$	$10\bar{1}1$		19	$2\bar{1}\bar{1}3$	$\bar{1}011$				
	8	$2\bar{1}\bar{1}0$	$01\bar{1}1$		20	$11\bar{2}3$	$\bar{1}011$				
	9	$11\bar{2}0$	$\bar{1}101$		21	$11\bar{2}3$	$0\bar{1}11$				
	10	$\bar{1}2\bar{1}0$	$\bar{1}011$		22	$\bar{1}2\bar{1}3$	$0\bar{1}11$				
	11	$\bar{2}110$	$0\bar{1}11$		23	$\bar{1}2\bar{1}3$	$1\bar{1}01$				
	12	$\bar{1}\bar{1}20$	$1\bar{1}01$		24	$\bar{2}113$	$1\bar{1}01$				

Table 2 Material parameters of single-crystal 6H-SiC

Parameter	Definition		Values	Data from [17]	Unit
C_{11}			325	501	GPa
C_{12}			60	111	GPa
C_{13}	Elastic constants		34	52	GPa
C_{33}			367	553	GPa
C_{44}			109	163	GPa
$\dot{\gamma}_0$	Reference shear rate		0.01		s^{-1}
n	Rate-sensitivity parameter		80		-
q	Latent hardening ratio		1.0		-
τ_0	Basal and Prismatic	Initial slip resistance	9.85	4.8	GPa
τ_s		Saturated slip resistance	15		GPa
h_0		Initial hardening modulus	9		GPa
τ_0	Pyramidal <a> 1st & 2nd order <c+a>	Initial slip resistance	11	4.8	GPa
τ_s		Saturated slip resistance	15		GPa
h_0		Initial hardening modulus	9		GPa

5 Results and discussion

5.1 Load-displacement curves

A comparison of load-displacement curves obtained from the experiment and simulations of indentation in two orientations are shown in Fig. 4. Our numerical efforts show a reasonable match to experimental results. Interestingly, simulations based on data from [17] show a noticeable difference when compared to experimental results for both orientations. Simulation result based on the data from our study for orientation 1 is a close match to experiments since model calibration tests were based on this particular experiment. For orientation 2, our numerical results show a slight deviation in the loading-unloading graph at higher loads; however, the residual displacement shows a close match to experiments (i.e. displacement at end of unloading step). Numerical results based on data in [17] show deviation both in load-displacement response as well as in the prediction of residual imprint.
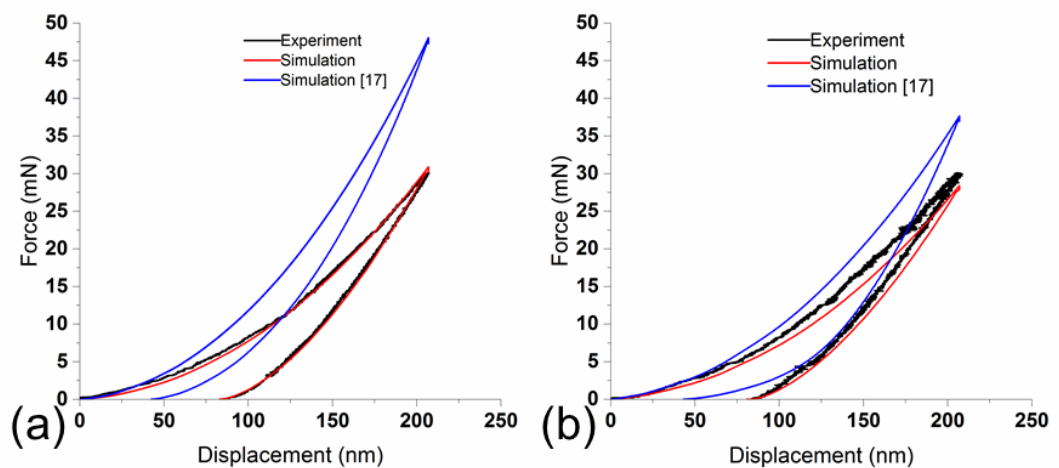
Fig. 4 Comparison of experimental and numerical load-displacement behaviour at (a) orientation 1 and (b) orientation 2 for Simulation: based on calibrated data and Simulation [17]: based on simulation results from data provided in [17].

5.2 Topography analysis

Next, we characterise the residual indentation imprint in orientation 1 (i.e. on the (0001) basal plane) with the use of AFM. Figure 5(a), (b) shows the AFM image of the residual imprint in the indented sample. There is no observable crack at the maximum imposed load of 30 mN, which confirms that plastic deformation dominates. Figure 5(c) is the surface profile obtained from the FE model. A comparison between the profiles along path A-B as indicated in Fig.5(b) from the experiment, and, path C-D in Fig.5(c) from the simulation is shown in Fig. 6. There is a reasonable match in the asymmetric profiles with the residual depth showing a good correlation between simulations and experiments.
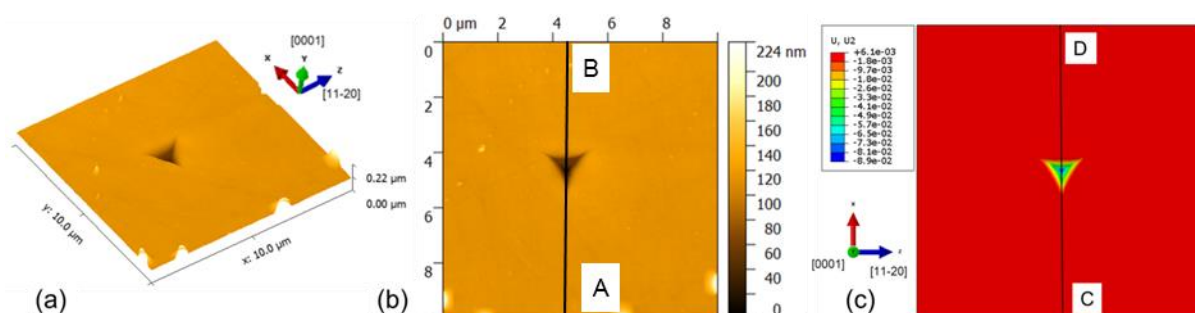

Fig. 5 AFM image of the 30 mN indent on orientation 1 (a) orthogonal view (b) top view and (c) simulated height profile of the nanoindent impression on single-crystal 6H-SiC work piece with Berkovich indenter on (0001) plane.
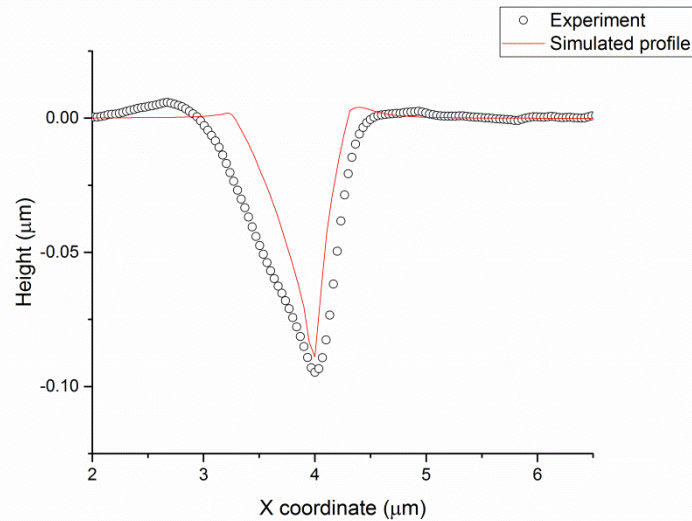
Fig. 6 Comparison of the profiles of the imprint between experiment and simulation

5.3 Slip system activation

The computation modelling framework can be used to probe the exact nature of slip system activation during the indentation process as a function of orientation. Figure 7 shows the accumulative shear strain, γ , in orientation 1 and 2 at the final steps of the simulation. For clarity, the local area of the indented region is shown here. Although there is no significant difference from the macroscopic responses of the experiment (i.e. load-displacement curves in Fig.4), the numerical results indicate that the microscopic responses (i.e. the sum of the absolute value of the shear strain across all slip systems) in the two chosen orientations are different. In orientation 1, the accumulative shear strain is higher than that of orientation 2. The simulation provide some insight into the activation of slips systems that experiments cannot capture. The microscopic response of the indented surface in terms of slip on each slip systems is further investigated.
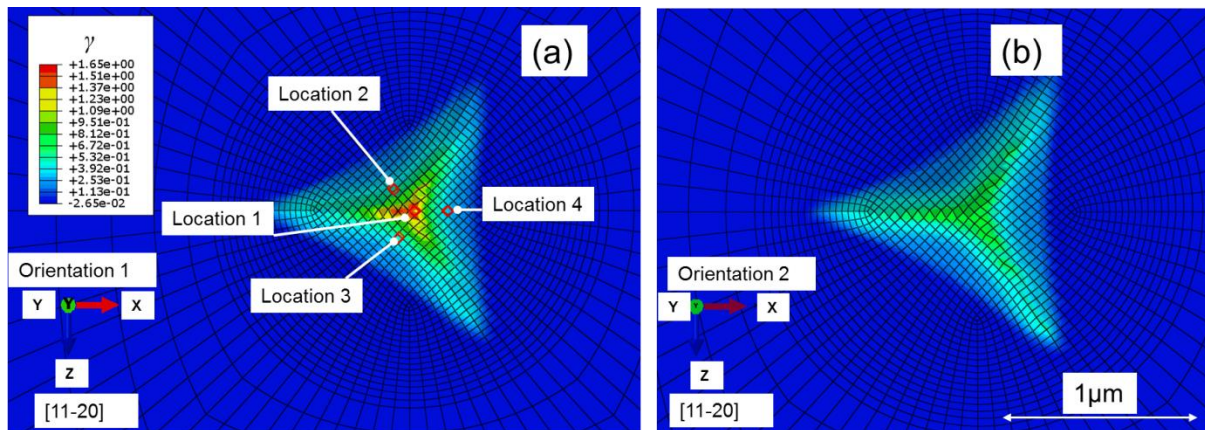
Fig.7 Contour plot of accumulative shear strain over all slip systems, γ, on (a) orientation 1 and (b) orientation 2. The local indented region is shown here for clarity

We choose four locations (labelled as Location 1-4 in Fig. 7(a)) in the vicinity of the indentation imprint, including the area directly under the indenter tip and in the middle of each faces of the imprint, for orientation 1 and orientation 2. Magnitudes of slip for all slip systems are quantified at these four locations and represented in Fig.8. For the selected locations, although there is moderate activations in basal plane (#1-3), majority of slip activation was found to be in the pyramidal $<c+a>$ 1st and 2nd order family (# 13-30), which indicate that pyramidal $<c+a>$ family dominate the deformation behaviour for orientation 1 especially at the vicinity of the indented region. Noticeably, at location 1 there is significant activation on slip systems #26 and #28, which corresponds to $[\bar{1}2\bar{1}3](1\bar{2}12)$ and $[\bar{2}113](2\bar{1}\bar{1}2)$ respectively. For orientation 2, the slip activation of basal family in location 1 is the highest among all other locations. The result agrees with the literature [17] that basal slip activates favourably just under the indenter tip due to it inducing the highest indentation Schmid factor. However, our studies show that the activation of slip system is rather complicated with activation of the pyramidal family being significant.

Another observation is that the prismatic (#4-6) and pyramidal $<a>$ (#7-12) have little activation especially for orientation 1. This may be due to high aspect ratio of the lattice constant (c/a =4.942) when compared to traditional HCP metallic materials. There is a greater

propensity for slip systems with a component in the *c*-axis to be activated earlier than the slip
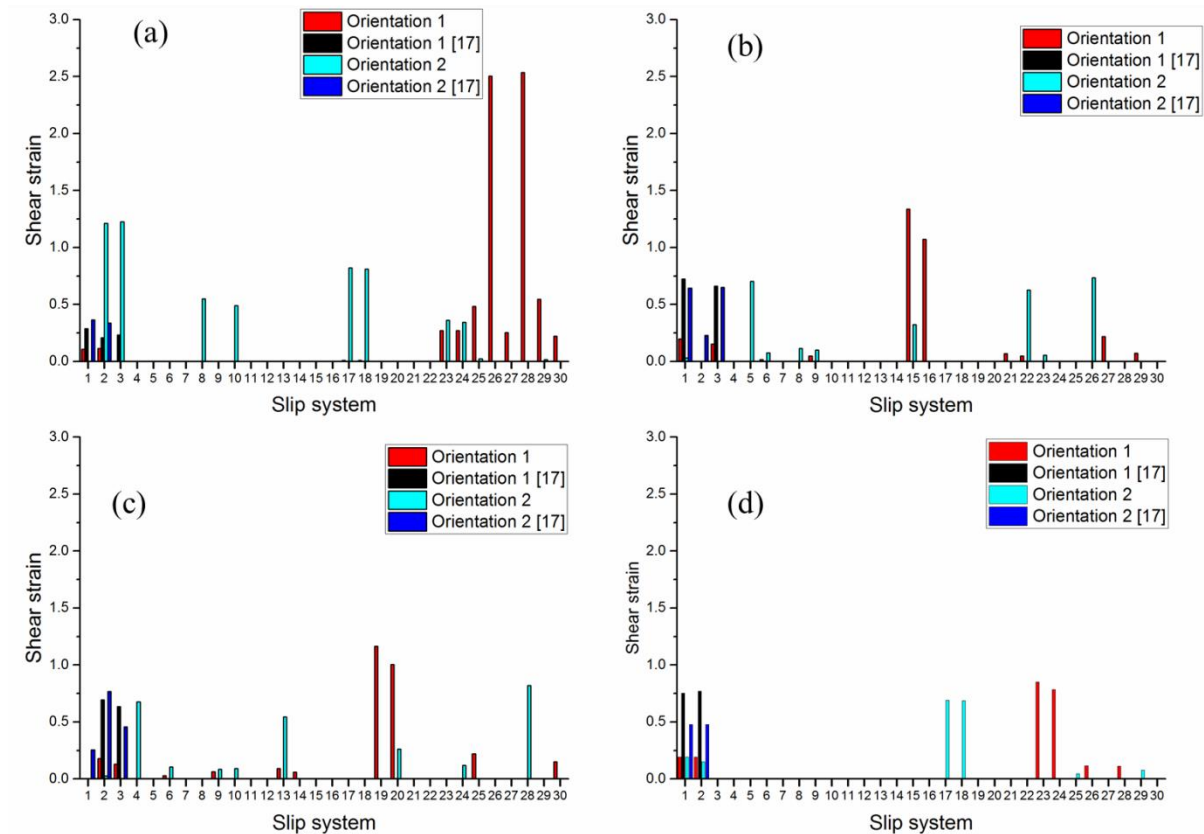
systems along the *a*-axis.

Fig.8 Slip systems activation comparison of orientation 1 and 2 based on calibrated data from

our study and data obtained from [17] at (a) Location 1, (b) Location 2, (c) Location 3 and (d)

Location 4

Our numerical studies significantly deviate from the predictions based on results presented in

Datye et. al [17]. The claim that basal slip dominants with other systems contributing mini-

mally to the perceived orientation induced anisotropy is probably not correct. The compari-

son of load displacement curve as well as surface topography analysis to experiments shown

that our modelling approach can reasonably elucidate the underlying principles of defor-

mation in the material. We appreciate the differences between the CRSS values we chose to

that presented in [17]. This may be due to differences in the specifics of the manufacturing process of the sample or perhaps due to apparent machine compliance. We would like to emphasize that most studies to date focus primarily on basal slip behaviour. We have intentionally applied a higher CRSS for the pyramidal slip systems, which are generally believed to be harder to activate, compare with basal and prismatic systems and yet our models indicate that slip activation of the pyramidal systems $<c+a>$ contribute significantly to deformations under the studied loading condition. Hence, activation of slip systems other that basal together with the high aspect ratio of lattice constant should be taken into account for modelling deformation response in 6H-SiC.

6 Concluding Remarks

This paper presents experimental and numerical results of nanoindentation in single-crystal 6H-SiC. A numerical implementation of a crystal plasticity theory on HCP like ceramic material was shown to capture experimental results reasonably well. Predictions from our model suggested that dislocation in the pyramidal $<c+a>$ families dominated the plastic deformation in nanoindentation process locally. The high aspect ratio of the lattice constants of single-crystal 6H-SiC could be the reason of high slip activation on the pyramidal $<c+a>$ families and low slip activation on the basal, prismatic and pyramidal $<a>$ planes comparatively. Thus considering all slip systems in deformation prediction of 6H-SiC especially with regard to local fields is important.

We have performed some preliminary TEM studies in the sample post indentation. We observe a noticeable increase in dislocation density especially under the indentation tip, which reinforces the importance of dislocation induced plasticity in the material at the small length scales. We are currently extending the modelling framework to capture dynamic effects which are particularly relevant in machining conditions. In the near future, we shall report on nano-scratching experiments and an appropriate numerical model to capture the underlying deformation conditions.

Acknowledgement

Reference

[1]   Kim S, Choi J, Jung M, Joo S, Kim S. Silicon carbide-based hydrogen gas sensors for high-temperature applications. Sensors (Basel) 2013;13:13575–83. doi:10.3390/s131013575.

[2]   Ortiz AL, Sánchez-Bajo F, Cumbrera FL, Guiberteau F. The prolific polytypism of silicon carbide. J Appl Crystallogr 2013;46:242–7. doi:10.1107/S0021889812049151.

[3]   Mehregany M, Zorman CA. SiC MEMS: opportunities and challenges for applications in harsh environments. Thin Solid Films 1999;355:518–24. doi:10.1016/S0257-8972(99)00374-6.

[4]   Phan H-P, Dao DV, Nakamura K, Dimitrijev S, Nguyen N-T. The Piezoresistive Effect of SiC for MEMS Sensors at High Temperatures: A Review. J Microelectromechanical Syst 2015;24:1663–77. doi:10.1109/JMEMS.2015.2470132.

[5]   Goel S, Luo X, Comley P, Reuben RL, Cox A. Brittle–ductile transition during diamond turning of single crystal silicon carbide. Int J Mach Tools Manuf 2013;65:15–21. doi:10.1016/j.ijmachtools.2012.09.001.

[6]   Goel S. The current understanding on the diamond machining of silicon carbide. J Phys D Appl Phys 2014;47:243001. doi:10.1088/0022-3727/47/24/243001.

[7]   Zhanga C, Ohmori H, Kato T, Morita N. Evaluation of surface characteristics of ground CVD-SiC using cast iron bond diamond wheels. Precis Eng 2001;25:56–62. doi:10.1016/S0141-6359(00)00056-8.

[8]   Yin L, Vancoille EYJ, Ramesh K, Huang H. Surface characterization of 6H-SiC (0001) substrates in indentation and abrasive machining. Int J Mach Tools Manuf 2004;44:607–15. doi:10.1016/j.ijmachtools.2003.12.006.

[9]   Meng B, Zhang Y, Zhang F. Material removal mechanism of 6H-SiC studied by nano-scratching with Berkovich indenter. Appl Phys A 2016;122:247. doi:10.1007/s00339-016-9802-7.

[10]   Meng B, Zhang F, Li Z. Deformation and removal characteristics in nanoscratching of 6H-SiC with Berkovich indenter. Mater Sci Semicond Process 2015;31:160–5. doi:10.1016/j.mssp.2014.11.034.

[11]   Patten J, Gao W, Yasuto K. Ductile Regime Nanomachining of Single-Crystal Silicon Carbide. J Manuf Sci Eng 2005;127:522. doi:10.1115/1.1949614.

[12]   Yan J, Zhang Z, Kuriyagawa T. Mechanism for material removal in diamond turning of reaction-bonded silicon carbide. Int J Mach Tools Manuf 2009;49:366–74. doi:10.1016/j.ijmachtools.2008.12.007.

[13]   Xiao G, To S, Zhang G. The mechanism of ductile deformation in ductile regime machining of 6H SiC. Comput Mater Sci 2015;98:178–88. doi:10.1016/j.commatsci.2014.10.045.

[14]   Yan J, Gai X, Harada H. Subsurface Damage of Single Crystalline Silicon Carbide in Nanoindentation Tests. J Nanosci Nanotechnol 2010;10:7808–11. doi:10.1166/jnn.2010.2895.

[15]   Page TF, Oliver WC, McHargue CJ, Newey D, Wilkins MA, Pollock HM, et al. The deformation behavior of ceramic crystals subjected to very low load (nano)indentations. J Mater Res 1992;7:450–73. doi:10.1557/JMR.1992.0450.

[16]   Page TF, Riester L, Hainsworth S V., Minomura S, Drickamer HG, Morris JC, et al. The Plasticity Response Of 6H-Sic and Related Isostructural Materials to Nanoindentation: Slip vs Densification. MRS Proc 1998;522:113. doi:10.1557/PROC-522-113.

[17]   Datye A, Li L, Zhang W, Wei Y, Gao Y, Pharr GM. Extraction of Anisotropic Mechanical Properties From Nanoindentation of SiC-6H Single Crystals. J Appl Mech 2016;83:91003. doi:10.1115/1.4033790.

[18]   Tymicki E, Grasza K, Diduszko R, Bożek R, Gała M. Initial stages of SiC crystal growth by PVT method. Cryst Res Technol 2007;42:1232–6. doi:10.1002/crat.200711011.

[19]   Staroselsky AV. 1962-. Crystal plasticity due to slip and twinning 1998.

[20]   Staroselsky A, Anand L. A constitutive model for hcp materials deforming by slip and twinning. Int J Plast 2003;19:1843–64. doi:10.1016/S0749-6419(03)00039-1.

[21]   Liu Q, Roy A, Silberschmidt V V. Temperature-dependent crystal-plasticity model for magnesium: A bottom-up approach. Mech Mater 2017;113:44–56. doi:https://doi.org/10.1016/j.mechmat.2017.07.008.

[22]   Gao YF, Larson BC, Lee JH, Nicola L, Tischler JZ, Pharr GM. Lattice Rotation Patterns and Strain Gradient Effects in Face-Centered-Cubic Single Crystals Under Spherical Indentation. J Appl Mech 2015;82:61007. doi:10.1115/1.4030403.

[23]   Demiral M, Roy A, El Sayed T, Silberschmidt V V. Influence of strain gradients on lattice rotation in nano-indentation experiments: A numerical study. Mater Sci Eng A 2014;608:73–81. doi:10.1016/j.msea.2014.04.033.

[24]   Liu Q, Demiral M, Roy A, Silberschmidt V V. Modelling and Simulations of Nanoindentation in Single Crystals. Appl. Nanoindentation Adv. Mater., John Wiley & Sons, Ltd; 2017, p. 561–77. doi:10.1002/9781119084501.ch23.

[25]   Liu Q, Roy A, Tamura S, Matsumura T, Silberschmidt V V. Micro-cutting of single-crystal metal: Finite-element analysis of deformation and material removal. Int J Mech Sci 2016;118:135–43. doi:10.1016/j.ijmecsci.2016.09.021.

[26]   Huang Y. A User-material Subroutine Incoporating Single Crystal Plasticity in the ABAQUS Finite

Element Program. Harvard Univ 1991.

[27]   Hutchinson JW. Bounds and Self-Consistent Estimates for Creep of Polycrystalline Materials. Proc R Soc London A Math Phys Eng Sci 1976;348.

[28]   Peirce D, Asaro RJ, Needleman A. An analysis of nonuniform and localized deformation in ductile single crystals. Acta Metall 1982;30:1087–119. doi:10.1016/0001-6160(82)90005-0.

[29]   Asaro RJ. Crystal Plasticity. J Appl Mech 1983;50:921. doi:10.1115/1.3167205.

[30]   Asaro RJ. Micromechanics of Crystals and Polycrystals. vol. 23. Elsevier; 1983. doi:10.1016/S0065-2156(08)70242-4.

[31]   Sánchez-Martín R, Pérez-Prado MT, Segurado J, Bohlen J, Gutiérrez-Urrutia I, Llorca J, et al. Measuring the critical resolved shear stresses in Mg alloys by instrumented nanoindentation. Acta Mater 2014;71:283–92. doi:10.1016/j.actamat.2014.03.014.

[32]   Kwon G, Jo H-H, Lim S, Shin C, Jin H-H, Kwon J, et al. Room-temperature yield and fracture strength of single-crystalline 6H silicon carbide. J Mater Sci 2015. doi:10.1007/s10853-015-9379-0.